

High-harmonic spectroscopy of ultrafast many-body dynamics in strongly correlated systems

R. E. F. Silva^{1*}, Igor V. Blinov^{2,3}, Alexey N. Rubtsov^{2,4}, O. Smirnova^{1,5} and M. Ivanov^{1,6,7*}

We bring together two topics that, until now, have been the focus of intense but non-overlapping research efforts. The first concerns high-harmonic generation in solids, which occurs when an intense light field excites a highly non-equilibrium electronic response in a semiconductor or a dielectric. The second concerns many-body dynamics in strongly correlated systems such as the Mott insulator. We show that high-harmonic generation can be used to time-resolve ultrafast many-body dynamics associated with an optically driven phase transition, with accuracy far exceeding one cycle of the driving light field. Our work paves the way for time-resolving highly non-equilibrium many-body dynamics in strongly correlated systems, with few femtosecond accuracy.

High-harmonic emission provides the frequency-domain view of charge dynamics in quantum systems¹. Complete characterization of emitted harmonic light—its spectrum, polarization and spectral phase—allows one to decode the underlying charge dynamics in atoms and molecules with a resolution of <0.1 fs, well below a single cycle of the driving laser field, opening up the field of ultrafast high-harmonic spectroscopy^{2–9}. In particular, harmonic generation in gases reveals the importance of multi-electron correlations^{8,10,11}, showing enhanced emission near giant resonances in photo-absorption^{10,11} or enhanced tunnelling⁸.

Here, we bring together high-harmonic spectroscopy and many-body dynamics in strongly correlated solids, focusing on an ultrafast phase transition. We consider the breakdown of the Mott insulating state in the canonical model of a strongly correlated solid, the Fermi–Hubbard model. We show how the complex many-body charge dynamics underlying this transition are recorded by high harmonic emission, with ~ 1 fs accuracy.

Combining high-harmonic generation (HHG) in bulk solids^{12–16} with robust techniques for characterizing emitted light^{14–16} opens up new opportunities. Recent results include the demonstration of dynamical Bloch oscillations^{16,17}, reconstruction of the band-structure in ZnO¹⁸, visualization of strong field-induced effective band-structure¹⁹, direct visualization of the asymmetric charge flow driven by mid-infrared (mid-IR) fields²⁰ and the first steps towards measuring the Berry curvature²¹. These studies have focused on systems well described by a single-particle band-structure, and single-particle pictures have dominated analyses (for example, refs^{12–14,16,19,22}). Two harmonic generation mechanisms emerging in the single-particle picture are associated with intra-band current and inter-band polarization. Their relative role is hotly debated (see, for example, refs^{12–18,23,24}). Electron–electron correlations have often been incorporated via empirically introduced (and surprisingly short—only a few femtoseconds) relaxation times (for example, refs^{13,14,23}).

Theoretical studies explicitly including electron–electron interactions (for example, refs^{24,25}) reveal a more complex picture—the harmonic spectra were found to be robust with respect to elastic and inelastic scattering²⁵, and electron exchange and interaction do not appear to yield ‘clean’ harmonic spectra²⁴, in contrast to simple relaxation models.

Indeed, electron–electron correlations go well beyond mere dephasing, generating rich physics of strongly correlated systems, such as pre-thermalization and the formation of extended Gibbs ensembles²⁶, and the superfluid to Mott insulator transition²⁷, to name but a few. Studies of non-equilibrium many-body dynamics have led to the concepts of dynamical²⁸ and light-induced phase transitions^{29–32}. In particular, the Mott insulator-to-metal transition was recently achieved experimentally in VO₂ (refs^{31,32}). However, resolving such transitions with few-femtosecond accuracy remains elusive. Our results show that high-harmonic spectroscopy offers a detailed view of the underlying dynamics with a resolution of ~ 1 fs.

Here, we use a one-dimensional Fermi–Hubbard model with half-filling, that is, one particle per site on average (see Methods). A particle could hop to an adjacent site with a rate t_0 . Hopping can be obstructed by another particle already residing on this site, via the energy U of the repulsive on-site interaction. In the strong coupling limit $U \gg t_0$, the Mott insulating ground state has short-range antiferromagnetic order³³ (electron spins at adjacent sites tend to be anti-parallel). The elementary charge excitations, called doublon–hole pairs^{34,35}, are separated by an optical gap Δ . When $U \gg t_0$, Δ scales linearly with U . We focus on this regime. The laser frequency $\omega_L \ll \Delta(U)$ is in the mid-IR range, with $\omega_L = 32.9$ THz identical to that in recent experiments¹⁴, and a modest field amplitude of $F_0 = 10$ MV cm⁻¹. The hopping rate $t_0 = 0.52$ eV mimics that of Sr₂CuO₃ (ref.³⁴). U is varied to demonstrate the trends and the general nature of our conclusions. For simulation details see Methods.

To induce and resolve the Mott transition, we apply a light pulse where the field amplitude $F_0(t)$ increases smoothly. This field can excite the doublon–hole pairs, which play the role of charge carriers. The density of doublon–hole pairs may change during the pulse, depending on the field amplitude $F_0(t)$. As $F_0(t)$ crosses the threshold F_{th} , the density of charge carriers exceeds a critical value, leading to breakdown of the Mott insulator. The transition is followed by destruction of local short-range magnetic order, and a paramagnetic liquid-like state is formed^{30,34}. Smooth variation of $F_0(t)$ during the pulse allows us to track the transition as a function of time. The transition is mathematically similar to strong-field ionization in atoms³⁴; the parameter $\gamma = \hbar\omega_L/\xi F_0$ (where ξ is the correlation length³⁴) serves as the analogue of the Keldysh adiabaticity parameter¹. In the ‘tunnelling’ regime $\gamma \ll 1$, the threshold field is given by³⁴

¹Max-Born-Institut, Berlin, Germany. ²Russian Quantum Center, Skolkovo, Russia. ³Moscow Institute of Physics and Technology, Dolgoprudny, Moscow, Russia. ⁴Department of Physics, Moscow State University, Moscow, Russia. ⁵Technische Universität Berlin, Ernst-Ruska-Gebäude, Berlin, Germany.

⁶Blackett Laboratory, Imperial College London, South Kensington Campus, London, UK. ⁷Department of Physics, Humboldt University, Berlin, Germany.

*e-mail: silva@mbi-berlin.de; mikhail.ivanov@mbi-berlin.de

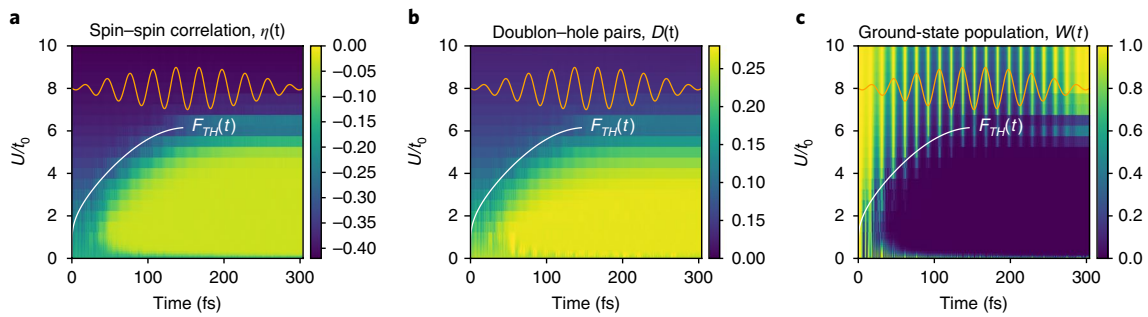


Fig. 1 | Time-resolved light-induced breakdown in the Mott insulator. a, b, Time-resolved spin-spin correlation (**a**) and number of doublon-hole pairs (**b**) for a range of U/t_0 . The pulse has peak strength $F_0 = 10 \text{ MV cm}^{-1}$, frequency 32.9 THz , and a 10-cycle-long \sin^2 envelope. The red curve shows the time when the threshold field strength for the transition is reached. The field amplitude is insufficient for the breakdown at $U/t_0 > 6$, in agreement with F_{th} from equation (1). **c**, Abrupt destruction of the Mott state, shown via $W(t) = |\langle \Psi_0 | \Psi(t) \rangle|^2$, where Ψ is the many-body wavefunction, occurs within a cycle for fields exceeding the threshold.

$$F_{th} = \Delta / 2e\xi \tag{1}$$

We will characterize the state of the system via the two parameters describing the charge and spin degrees of freedom, to give the next-neighbour spin-spin correlation function

$$\eta = \frac{1}{L} \left\langle \sum_{j=1}^L \mathbf{S}_j \cdot \mathbf{S}_{j+1} \right\rangle \tag{2}$$

and the average number of doublon-hole pairs per site

$$D = \frac{1}{L} \left\langle \sum_{j=1}^L c_{j,\uparrow}^\dagger c_{j,\uparrow} c_{j,\downarrow}^\dagger c_{j,\downarrow} \right\rangle \tag{3}$$

where j indicates the site, up and down arrows the spin, $L = 12$ is the number of sites, and c^\dagger, c are the creation and annihilation operators, respectively.

The destruction of short-range antiferromagnetic order during the transition is shown in Fig. 1a. Within a cycle, the spin-spin correlation function drops to nearly zero (limited by the finite size of the system). The second signature of the transition is the rise in the number of doublon-hole pairs (Fig. 1b), which is linked to the loss of spin-spin correlation (compare Fig. 1a,b). After the transition, the system reaches a photo-induced saturated state³⁴ and the num-

ber of pairs remains constant. The abrupt nature of the transition is shown in Fig. 1c: for fields crossing F_{th} the overlap probability with the initial state $W(t) = |\langle \Psi_0 | \Psi(t) \rangle|^2$ drops to zero within a laser cycle, stressing the need for sub-cycle resolution.

Naturally, the rise of optical charge excitations has to manifest in the optical response. Indeed, we find that the transition is accompanied by characteristic high-harmonic emission. Figure 2 shows harmonic spectra for different values of U/t_0 . In the conducting limit $U/t_0 = 0$ the emission is typical for a single-band tight-binding model¹². The harmonics are associated with the intra-band current, and they are narrow and well defined. Increasing electron correlation suppresses low-order harmonics and makes the spectra less regular (Fig. 2a).

For $U/t_0 \gg 1$ (Fig. 2b), the spectrum becomes quite unusual. First, in contrast to systems described by single-particle band-structures^{12-15,17,24}, where intra-band harmonics are very prominent²⁴, here the low-order intra-band harmonics are strongly suppressed at all times.

Second, the harmonic spectrum is rather irregular. Thus, electron-electron correlation does not just lead to fast dephasing, which would have yielded regular, narrow harmonic lines¹³. Note that the calculated emission is fully coherent: spectral complexity reflects the underlying dynamics.

Third, the harmonic spectrum shifts towards orders $N \sim U/\omega_L$. Figure 3a scans U/t_0 to demonstrate the trend. For $U/t_0 \gg 1$, the spectrum peaks near the characteristic energies of doublon-hole excitation. In the half-filled system, the first allowed excitations have energies between Δ and $\Delta + 8t_0$ (refs^{34,35}). Their range, shown

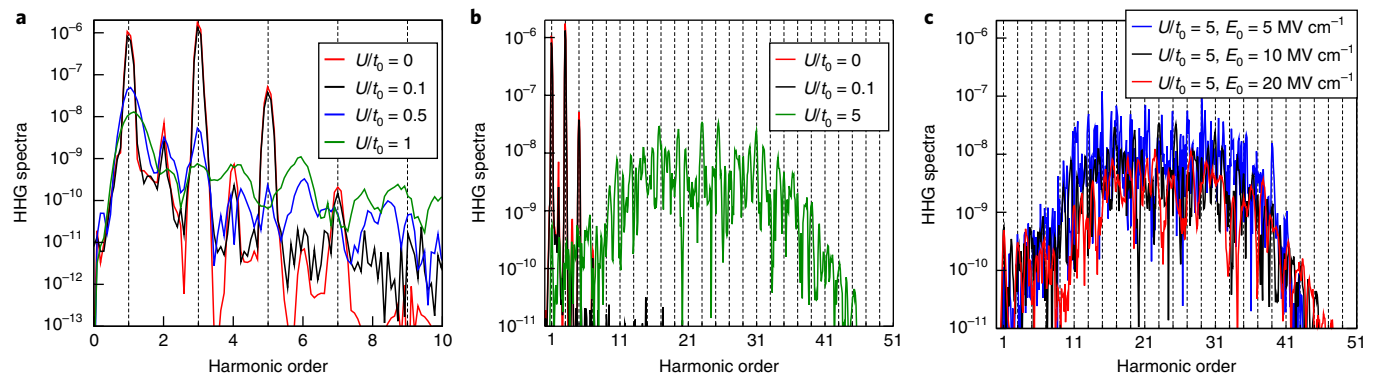


Fig. 2 | High-harmonic spectroscopy of light-induced transition in a strongly correlated system. a, Low-order harmonic spectra for $U/t_0 = 0, 0.1, 0.5$ and 1 . **b**, Harmonic spectra for the conducting state, $U/t_0 = 0$, weak correlation $U/t_0 = 0.1$ and the insulating state at $U/t_0 = 5$. Dashed lines show positions of odd harmonics. **c**, Dependence of the harmonic spectrum on the peak field, showing the same cutoff.

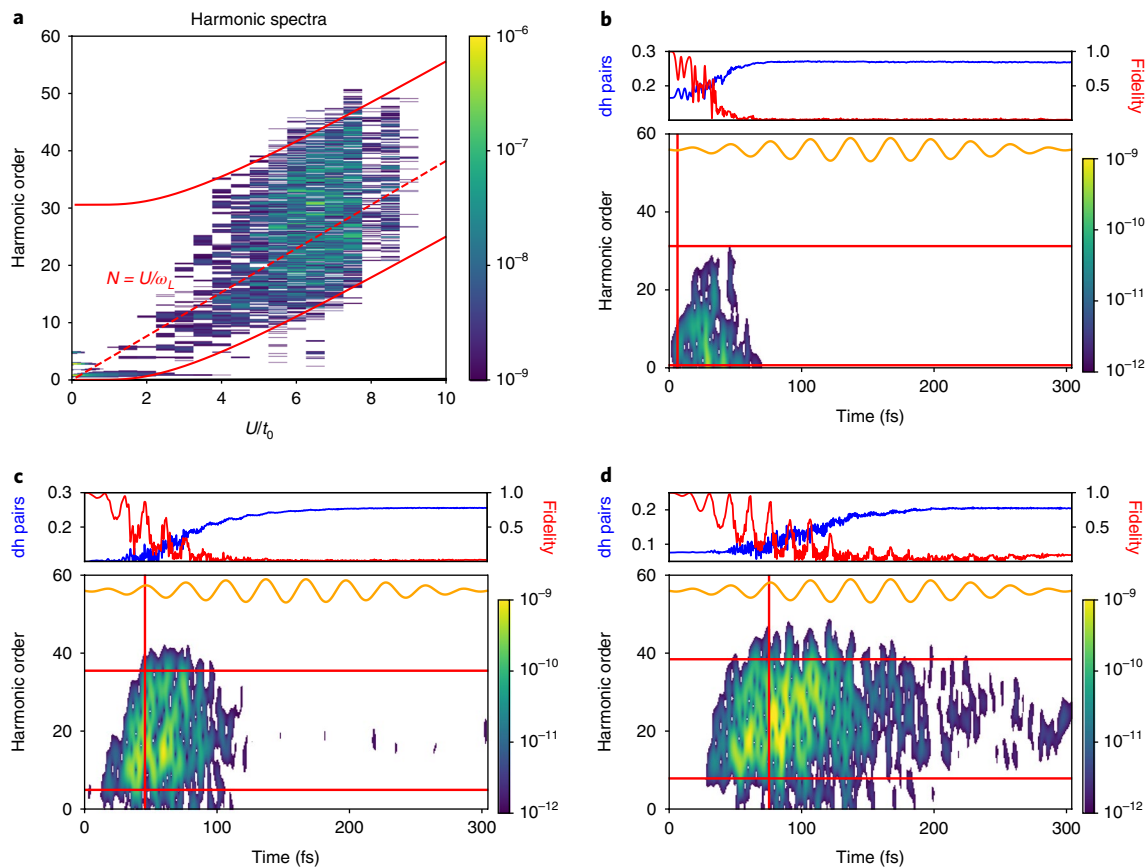


Fig. 3 | High-harmonic spectroscopy of light-induced transition in a strongly correlated system. **a**, High-harmonic spectrum as a function of U/t_0 . Note the change in the emission spectrum in the strong coupling limit $U \gg t_0$: low harmonics are absent, the emission peaks at the characteristic energy of doublon-hole excitation $\hbar\Omega - U$, shown with a dashed line. **b–d**, Gabor profiles of the harmonic signal for $U/t_0 = 2$ (**b**), $U/t_0 = 4$ (**c**) and $U/t_0 = 5$ (**d**). Vertical red lines show when the amplitude $F_0(t)$ exceeds the threshold field F_{th} for this value of U/t_0 . The two horizontal red lines indicate Δ and $\Delta + 8t_0$ for this U/t_0 . The top panels show the average number of doublon-hole (dh) pairs per site (blue) and the decay of the insulating ground-state fidelity $\Xi(t) = |\langle \Psi_0 | \Psi(t) \rangle|$ (red).

with red lines in Fig. 3a, defines the lower and upper frequencies for the harmonic emission. Figure 2c shows that the range of emitted energies and the cutoff are field-independent (once the threshold for the transition is crossed). Thus, Figs. 2c and 3 suggest that emission is dominated by one-photon transitions back to the original ground state via a single doublon-hole recombination.

This conclusion is confirmed in Fig. 3b–d, which shows the time profiles of harmonic emission, obtained via the Gabor transform (see Methods). Note that similar time–frequency spectrograms of the emitted harmonic light with ~ 1 – 2 fs accuracy are now experimentally available¹⁴ for the same laser parameters as used in our calculation. We see that (1) the onset of harmonic emission is synchronized with breakdown of the insulating Mott state and the rise in the number of doublon-hole pairs, and (2) the fall in emission follows depletion of the ground-state state (Fig. 3b–d), following the fidelity $\Xi(t) = |\langle \Psi_0 | \Psi(t) \rangle|$ (upper parts in Fig. 3b–d). The Gabor profiles in Fig. 3b–d show that the emission takes ~ 50 – 70 fs, that is, only about 1–2 cycles of the driving field. Rapid rise and fall of the emission reflects the lack of periodicity of the excited many-body dynamics (studied further in Fig. 4).

To analyse the excitation dynamics, we projected the exact wavefunction onto the subspaces corresponding to one-hole excitations, two-hole excitations, and so on, obtaining the corresponding components $|\psi_i(t)\rangle$, where i is the number of doubly occupied sites. Figure 4a shows the flow of populations $P_i(t)$ between these different subspaces. Note that for the chosen finite value of $U/t_0 = 5$, the

ground state contains components with $i = 1, 2, 3$. As the ground state is depleted, the population is rapidly transferred to subspaces with $i = 2, 3, 4$. Now, we compute the contributions $J_{ji} = \langle \psi_j | j | \psi_i \rangle + c.c.$ to the total coherent emission. We see that the dominant contributions come from the coherences between the subspaces that were already present in the ground state (Fig. 4b–d). Indeed, the rise of these coherences coincides with the onset of excitation, while their fall follows depletion of the ground state (Fig. 4a). Excitation to ‘new’ subspaces, for example $i = 4$ (absent in the ground state) does not lead to any substantial coherent emission. In spite of substantial population of $i = 3, 4$ coupled via a single-photon transition, $J_{4,3}$ (Fig. 4d) is two to three orders of magnitude weaker than, for example, $J_{2,1}$ (compare Fig. 4b,d, note the scale in Fig. 4d).

Interestingly, for a pair of subspaces coupled by one-photon transition, there is some emission at energies above the maximum gap between the ground state and the first Hubbard band (Fig. 4b,c). However, when all contributions are added coherently, this emission is cancelled. Thus, for the whole many-body wavefunction, the only coherences that survive are between the excited components of the wavefunction and the ground state; strong electron–electron interaction suppresses coherences between the newly created excitations. The aperiodic behaviour of the ground-state population and excitations $P_i(t)$ during the transition are also likely reasons for the highly structured harmonic spectrum.

The cutoff of the harmonic signal does not scale linearly with the electric field, in contrast to single-particle band-structure systems in

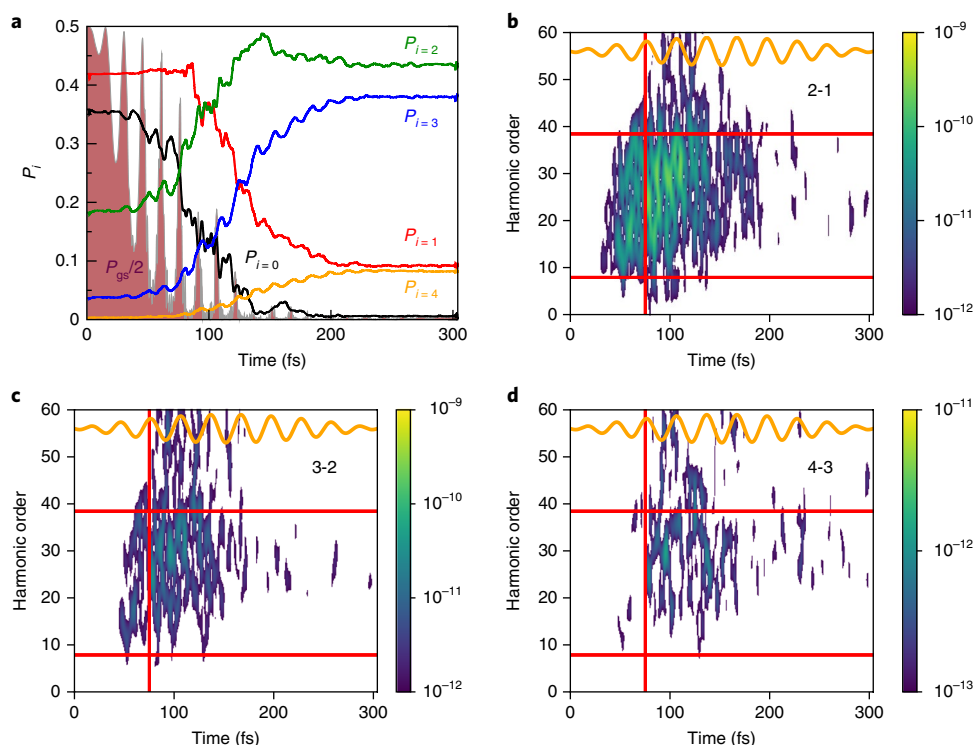


Fig. 4 | High-harmonic spectroscopy of light-induced transition in a strongly correlated system for $U/t_0 = 5$. **a**, Probability of having exactly i doubly occupied sites, $P_i = \langle \psi_i | \psi_i \rangle$. The ground-state population, divided by two, is shown as the purple shaded area. The results are convoluted with a 1 fs Gaussian. **b–d**, Time profiles of high-harmonic contributions from different components of the current J_{ij} : $i=1$ and $j=2$ (**b**), $i=2$ and $j=3$ (**c**) and $i=3$ and $j=4$ (**d**). Note the different scale in **d**.

moderate fields^{12,13,16,17}. Above the threshold $F_0 \geq F_{th}$, in the tunnelling regime all quasi-momenta for the doublon–hole pairs in the first Hubbard band are occupied³⁴, covering all available energies between Δ and $\Delta + 8t_0$, leading to similar spectra for different fields (Fig. 2c). The saturated state also does not support Bloch-like oscillations of doublon–hole pairs, leading to the loss of low-order harmonics.

HHG was pioneered three decades ago³⁶, evolving into the technological backbone of attosecond science¹ and a unique tool for ultrafast spectroscopy^{3,23}. Our work brings many-body dynamics in strongly correlated solids into its purview. Because high-harmonic emission characterizes coherent excitations, its time-resolved spectrum shows which excitations generate many-body coherences and which do not.

Methods

Methods, including statements of data availability and any associated accession codes and references, are available at <https://doi.org/10.1038/s41566-018-0129-0>.

Received: 26 June 2017; Accepted: 9 February 2018;

Published online: 26 March 2018

References

- Krausz, F. & Ivanov, M. Attosecond physics. *Rev. Mod. Phys.* **81**, 163–234 (2009).
- Baker, S. et al. Probing proton dynamics in molecules on an attosecond time scale. *Science* **312**, 424–427 (2006).
- Lein, M. Molecular imaging using recolliding electrons. *J. Phys. B* **40**, R135–R173 (2007).
- Smirnova, O. et al. High harmonic interferometry of multi-electron dynamics in molecules. *Nature* **460**, 972–977 (2009).
- Haessler, S. et al. Attosecond imaging of molecular electronic wavepackets. *Nat. Phys.* **6**, 200–206 (2010).
- Shafir, D. et al. Resolving the time when an electron exits a tunnelling barrier. *Nature* **485**, 343–346 (2012).
- Pedatzur, O. et al. Attosecond tunnelling interferometry. *Nat. Phys.* **11**, 815–819 (2015).
- Bruner, B. D. et al. Multidimensional high harmonic spectroscopy of polyatomic molecules: detecting sub-cycle laser-driven hole dynamics upon ionization in strong mid-IR laser fields. *Faraday Discuss.* **194**, 369–405 (2016).
- Kraus, P. M. et al. Measurement and laser control of attosecond charge migration in ionized iodoacetylene. *Science* **350**, 790–795 (2015).
- Shiner, A. et al. Probing collective multi-electron dynamics in xenon with high-harmonic spectroscopy. *Nat. Phys.* **7**, 464–467 (2011).
- Pabst, S. & Santra, R. Strong-field many-body physics and the giant enhancement in the high-harmonic spectrum of xenon. *Phys. Rev. Lett.* **111**, 233005 (2013).
- Ghimire, S. et al. Observation of high-order harmonic generation in a bulk crystal. *Nat. Phys.* **7**, 138–141 (2011).
- Vampa, G. et al. Theoretical analysis of high-harmonic generation in solids. *Phys. Rev. Lett.* **113**, 073901 (2014).
- Hohenleutner, M. et al. Real-time observation of interfering crystal electrons in high-harmonic generation. *Nature* **523**, 572–575 (2015).
- Langer, F. et al. Lightwave-driven quasiparticle collisions on a subcycle timescale. *Nature* **533**, 225–229 (2016).
- Luu, T. T. et al. Extreme ultraviolet high-harmonic spectroscopy of solids. *Nature* **521**, 498–502 (2015).
- Schubert, O. et al. Sub-cycle control of terahertz high-harmonic generation by dynamical Bloch oscillations. *Nat. Photon.* **8**, 119–123 (2014).
- Vampa, G. et al. All-optical reconstruction of crystal band structure. *Phys. Rev. Lett.* **115**, 193603 (2015).
- Hawkins, P. G., Ivanov, M. Y. & Yakovlev, V. S. Effect of multiple conduction bands on high-harmonic emission from dielectrics. *Phys. Rev. A* **91**, 013405 (2015).
- You, Y. S., Reis, D. A. & Ghimire, S. Anisotropic high-harmonic generation in bulk crystals. *Nat. Phys.* **13**, 345–349 (2017).
- Liu, H. et al. High-harmonic generation from an atomically thin semiconductor. *Nat. Phys.* **13**, 262–265 (2017).
- Higuchi, T., Stockman, M. I. & Hommelhoff, P. Strong-field perspective on high-harmonic radiation from bulk solids. *Phys. Rev. Lett.* **113**, 213901 (2014).
- Vampa, G. & Brabec, T. Merge of high harmonic generation from gases and solids and its implications for attosecond science. *J. Phys. B* **50**, 083001 (2017).
- Tancogne-Dejean, N., Mücke, O. D., Kärtner, F. X. & Rubio, A. Impact of the electronic band structure in high-harmonic generation spectra of solids. *Phys. Rev. Lett.* **118**, 087403 (2017).

25. Kemper, A. F., Moritz, B., Freericks, J. K. & Devereaux, T. P. Theoretical description of high-order harmonic generation in solids. *New J. Phys.* **15**, 023003 (2013).
26. Eisert, J., Friesdorf, M. & Gogolin, C. Quantum many-body systems out of equilibrium. *Nat. Phys.* **11**, 124–130 (2015).
27. Bloch, I., Dalibard, J. & Zwerger, W. Many-body physics with ultracold gases. *Rev. Mod. Phys.* **80**, 885–964 (2008).
28. Heyl, M., Polkovnikov, A. & Kehrein, S. Dynamical quantum phase transitions in the transverse-field Ising model. *Phys. Rev. Lett.* **110**, 135704 (2013).
29. Nasu, K. *Photo-Induced Phase Transitions* (World Scientific, Hackensack, NJ, USA, 2004).
30. Oka, T. & Aoki, H. Photoinduced Tomonaga–Luttinger-like liquid in a Mott insulator. *Phys. Rev. B* **78**, 241104 (2008).
31. Liu, M. et al. Terahertz-field-induced insulator-to-metal transition in vanadium dioxide metamaterial. *Nature* **487**, 345–348 (2012).
32. Mayer, B. et al. Tunneling breakdown of a strongly correlated insulating state in VO₂ induced by intense multiterahertz excitation. *Phys. Rev. B* **91**, 235113 (2015).
33. Gebhard, F. *The Mott Metal–Insulator Transition: Models and Methods* (Springer, Berlin, Germany, 1997).
34. Oka, T. Nonlinear doublon production in a Mott insulator: Landau–Dykhne method applied to an integrable model. *Phys. Rev. B* **86**, 075148 (2012).
35. Essler, F. H. L., Frahm, H., Göhmann, E., Klümper, A. & Korepin, V. E. *The One-Dimensional Hubbard Model* (Cambridge Univ. Press, Cambridge, UK, 2010).
36. Ferray, M. et al. Multiple-harmonic conversion of 1064 nm radiation in rare gases. *J. Phys B* **21**, L31–L35 (1988).

Acknowledgements

The authors acknowledge fruitful discussions with T. Oka, B. Amorim and P. Hawkins. M.I. and R.E.F.S. acknowledge support from EPSRC/DSTL MURI grant EP/N018680/1.

Author contributions

R.E.F.S. developed the numerical code. M.I., R.E.F.S. and O.S. developed the idea. All authors contributed to analysis of the results. M.I. and R.E.F.S. wrote the main part of the manuscript, which was discussed by all authors.

Competing interests

The authors declare no competing interests.

Additional information

Reprints and permissions information is available at www.nature.com/reprints.

Correspondence and requests for materials should be addressed to R.E.F.S. or M.I.

Publisher's note: Springer Nature remains neutral with regard to jurisdictional claims in published maps and institutional affiliations.

Methods

We study HHG in the one-dimensional, half-filled Fermi–Hubbard model by exactly solving the time-dependent Schrödinger equation (TDSE) numerically, fully including the electron–electron correlations in the system interacting with the intense light field. We use the one-dimensional Fermi–Hubbard Hamiltonian³⁵

$$\hat{H}(t) = -t_0 \sum_{\sigma,j=1}^L (e^{-i\Phi(t)} c_{j,\sigma}^\dagger c_{j+1,\sigma} + e^{i\Phi(t)} c_{j+1,\sigma}^\dagger c_{j,\sigma}) + U \sum_{j=1}^L c_{j,\uparrow}^\dagger c_{j,\uparrow} c_{j,\downarrow}^\dagger c_{j,\downarrow} \quad (4)$$

where the laser electric field $F(t) = -dA(t)/dt$ enters through the time-dependent Peierls phase $eA(t) = -d\Phi(t)/dt$, $a = 7.56$ a.u. is the lattice constant, and $A(t)$ is the field vector potential. The hopping parameter t_0 is set to $t_0 = 0.52$ eV to mimic Sr_2CuO_3 (ref. ³⁴), and $U > 0$ is the on-site Coulomb repulsion. In the calculations, we use the periodic boundary conditions $c_{j,\sigma} = c_{j+L,\sigma}$ with $L = N = 12$, where N is the number of particles, and focus on the $S_z = 0$ subspace. Convergence of the harmonic emission and of the time evolution of the relevant observables used in this work were checked by performing the calculations for $L = N = 14$ and $U/t_0 = 2$,

4 and 5, yielding essentially the same results as for $L = N = 12$. Starting at $t = 0$ from the ground state of the Hamiltonian, we apply the pulse with $A(t) = A_0 f(t) \sin(\omega_L t)$ at the carrier wavelength of $9.11 \mu\text{m}$ ($\omega_L = 32.9$ THz) and the peak amplitude $F_0 = \omega_L A_0 = 10$ MV cm^{-1} . All the parameters of the pulse are well within experimental reach. The pulse has a total duration of 10 optical cycles and a sin^2 envelope, and is shown in Fig. 1.

To compute the harmonic emission, we first use the electric current operator, defined as³⁵

$$\hat{J}(t) = -ieat_0 \sum_{\sigma} \sum_{j=1}^L (e^{-i\Phi(t)} c_{j,\sigma}^\dagger c_{j+1,\sigma} - \text{h.c.}) \quad (5)$$

to compute the time-dependent current. The harmonic spectrum is calculated as the square of the Fourier transform of the dipole acceleration, $a(t) = \frac{d}{dt} J(t)$. Time-resolved emission is obtained by performing the Gabor (window Fourier) transform with the sliding window $\exp[-(t-\tau)^2/\sigma^2]$, $\sigma = (3\omega_L)^{-1}$.

Data availability. The data that support the plots within this paper and other findings of this study are available from the corresponding authors upon reasonable request.